ACS APPLIED MATERIALS & INTERFACES

www.acsami.org

Research Article

# Plasma Electroless Reduction: A Green Process for Designing Metallic Nanostructure Interfaces onto Polymeric Surfaces and 3D Scaffolds

Vineeth M. Vijayan, Melissa Walker, Renjith R. Pillai, Gerardo Hernandez Moreno, Yogesh K. Vohra, J. Jeffrey Morris, and Vinoy Thomas*

Cite This: https://doi.org/10.1021/acsami.2c01195

Read Online

ACCESS | Metrics & More | Article Recommendations | Supporting Information



**ABSTRACT:** The design of metal nanoparticle-modified polymer surfaces in a green and scalable way is both desirable and highly challenging. Herein, a new green low-temperature plasma-based *in situ* surface reduction strategy termed plasma electroless reduction (PER) is reported for achieving *in situ* metallic nanostructuring on polymer surfaces. Proof of concept for this new method was first demonstrated on hydrophilic cellulose papers. Cellulose papers were dip-coated with different metal ion ($Ag^{+}$ and $Au^{3+}$) solutions and then subjected to hydrogen plasma treatment for this PER process. Transmission electron microscopy (TEM) analysis has revealed that this PER process caused anisotropic growth of either gold or silver nanoparticles, resulting in the time-dependent formation of both distinct spherical nanoparticles (~20 nm) and anisotropic 2D nanosheets. Furthermore, we have demonstrated the adaptability of this process by applying it to hydrophobic fibrous and 3D printed polymeric materials such as surgical face masks and 3D printed polylactic acid scaffolds. The PER process on these hydrophobic polymer surfaces was accomplished via a sequential combination of air plasma and hydrogen plasma treatment. The metallic nanostructuring caused by the PER process on these hydrophobic surfaces was systematically studied using different surface imaging techniques including 3D confocal laser surface scanning microscopy and scanning electron microscopy. We have also systematically optimized the PER process on the surface of 3D scaffolds via varying the concentration of the silver ion precursor and by different postprocessing methods such as sonication and medium soaking. These optimization processes were found to be very important in generating uniform metallic nanoparticle-modified 3D printed scaffolds while simultaneously improving cytocompatibility. Through joint disk diffusion and inhibitory concentration testing, the antibacterial efficacy of silver coatings on face masks and 3D scaffolds was established. Altogether, these results clearly suggest the excellent futuristic potential of this new PER method for designing metallic nanostructured interfaces for different biomedical applications.

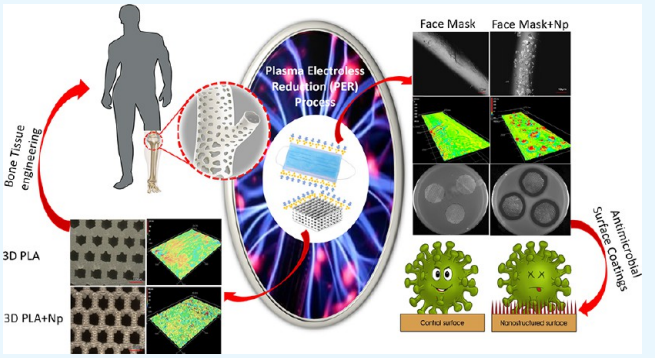


**KEYWORDS:** *metallic nanostructures, plasma electroless reduction, antimicrobial surfaces, face mask, 3D printed polymer scaffold*

## 1. INTRODUCTION

Gold and silver nanoparticles (AuNPs and AgNPs, respectively) represent one of the most important nanomaterials for biomedical applications.[1] They have been actively utilized to modify polymeric biomaterials, producing products such as antimicrobial surfaces, surface-modified tissue engineering scaffolds, and surface-enhanced Raman spectroscopy (SERS)-based biosensing devices.[2−4] Metallic NPs, when combined with polymers to form polymer−metal nanocomposites, have wide utility in biomedicine, making them indispensable in biomedical research. The design of such polymer−metal nanocomposites is accomplished via *in situ* and *ex situ* methods.[5] In the *in situ* method, the polymer matrix acts as a reaction medium for the formation of metallic NPs,[6] whereas in the *ex situ* method, the polymer matrix acts as a dispersion medium for the presynthesized NP.[7] The *in situ* method requires extremely hydrophilic systems such as hydrogels to prepare metal−polymer nanocomposites. The *ex situ* method is primarily applicable to viscoelastic thermoplastics in the high-temperature (≈200 °C) melt state.[5−7] This clearly shows that different factors such as hydrophilicity and high temperature are required for the preparation of polymer−metal nanocomposites. Apart from these polymer−metal nanocomposites,

Received: January 20, 2022
Accepted: May 19, 2022

metal NPs are also applied as surface coatings on polymer substrates via different techniques such as reversible addition−fragmentation chain transfer (RAFT) polymerization and electrochemical deposition.[8,9] More specifically, in RAFT polymerization, there are different approaches such as "grafting to" and "grafting from" to surface-modify the polymers with metallic NP such as AuNPs.[8] In the "grafting to" method, the polymer and the NPs are mixed and the polymer chains adsorb or bind covalently onto the NP surface.[10] In the "grafting from" method, the polymerization is carried out from a previously functionalized inorganic surface with the polymerization mediator.[11] However, both of these methods to prepare polymer−metal nanocomposites and metal nanocoatings require multiple steps, different chemical reagents (such as reducing, capping, and surface coupling agents), and can be efficiently applied only in polymers with hydrophilic surface characteristics. It is worth mentioning that many important polymeric biomaterials such as polypropylene (PP), polylactic acid (PLA), and polycaprolactone are hydrophobic in nature, as are the materials made from them (fibrous face masks, 3D printed scaffolds, and drug-eluting devices). The hydrophobicity of these polymer surfaces can seriously affect the NP modification process. As such, it is very important to explore new greener (without the usage of multiple chemical reagents having toxicity issues) and more robust (fast, economical, and easily scalable in industry settings) methods which can *in situ* surface-modify different polymer surfaces (hydrophilic and hydrophobic) with metallic nanostructures.

Plasma, the fourth state of matter (a partially ionized charged gas), represents one of the greener methods of synthesizing metallic NPs in a liquid phase.[12] Nonthermal low-temperature plasma (LTP) is a highly energetic state comprising ions, electrons, and radicals, which can interact and reduce the metallic precursors into metallic NPs.[13] Recently, nonthermal plasma was utilized to generate metallic NPs such as AuNPs and AgNPs at the liquid interface.[13,14] The electrons generated from plasma discharge reduce liquid-phase metallic salts into NPs. This particular process, however, only addresses the issue of toxicity secondary to the reducing agent. Issues such as overcoming hydrophobicity and the labor intensity still persist. Inspired by these unexplored problems, our present work reports a new green, efficient LTP-based *in situ* plasma electroless reduction (PER) strategy for generating metallic NPs on both hydrophilic and hydrophobic polymer surfaces without the use of electrodes, as seen in plasma electrolytic oxidation. Depending on the wettability of the substrate material, this *in situ* PER process can be accomplished using hydrogen plasma alone (for hydrophilic substrates) or a sequential combination of air plasma and hydrogen plasma treatment (for hydrophobic substrates). The PER nanometalized fibro-porous polymeric surfaces could be used for applications such as antimicrobial masks against COVID-19 for pandemic management[15,16] and for 3D scaffolds as bone−tissue interfacial scaffolds for osteomyelitis.[17]

## 2. EXPERIMENTAL SECTION

**2.1. Materials.** Silver(I) nitrate ($AgNO_3$) (Fisher Scientific, catalogue no S486-500, CAS no 7761-88-8, percent purity-99.8−100.5%) and gold(III) chloride tetrahydrate ($HAuCl_4{\cdot}3H_2O$) (Fisher Scientific, catalogue no G54-5, CAS no 16961-25-4, percent purity-≥49%) were used as the metallic salt precursors in this study. The Whatman qualitative cellulose filter paper, grade 1 (Millipore Sigma, catalogue no WHA1001325), was used as a hydrophilic substrate for the surface reduction process. The hydrophobic substrates used for the surface reduction process included a disposable surgical face mask [Jukang, model-MN-175, dimensions-175 mm × 95 mm, main ingredients: nonwoven fabric 70%/melt-blown cloth (filter) 30%] and 3D printed PLA scaffold printed using PLA filaments purchased from FlashForge USA (FlashForge 1.75 mm PLA 3D Printer Filament, 1 kg Spool). The Harrick Plasma chamber (PDC-001-HP) used for the *in situ* surface reduction process was purchased from Harrick Plasma, New York, USA. Hydrogen gas used for the *in situ* surface reduction process was purchased from Air Gas Company (Ultra High Purity Grade Hydrogen, Size 300 High Pressure Steel Cylinder, CGA-350).

**2.2. Methods.** For carrying out the PER process on hydrophilic cellulose filter paper, the paper was first dipped in 10 mL of 0.25 M or 250 mM $AgNO_3$ and 10 mL of 0.25 M or 250 mM $HauCl_4{\cdot}3H_2O$ solutions for 5 min. Afterward, the dip-coated substrates were placed inside a plasma chamber [Harrick Plasma chamber (PDC-001-HP)] with the following reaction conditions: a 13.56 MHz radiofrequency and a plasma power of 45 W. Hydrogen gas at a flow rate of 40 sccm was used to generate plasma inside the chamber for 10 min (a pressure of 500 mTorr was formed inside the chamber) to facilitate the surface reduction and subsequent formation of metallic nanostructures.

The PER process on hydrophobic materials such as surgical face masks was accomplished using an additional step of air plasma pretreatment. More specifically, the mask was exposed to air plasma pretreatment for 10 min (using a flow rate of 20 sccm with a radiofrequency 13.56 MHz, 45 W). After the air plasma pretreatment, the surgical mask was dip-coated in metal ion solutions ($AgNO_3$) and subjected to hydrogen plasma treatment using the same conditions as described above for the hydrophilic cellulose paper. After the plasma process, all the substrates were taken out and characterized with different techniques.

Time-dependent surface reduction on cellulose paper was carried out for time periods of 1, 3, and 5 min. In order to extract the NPs formed on the surface of the cellulose paper, these papers were cut into small pieces and dissolved in 5 mL of distilled water before being subjected to probe sonication for 15 min. The resultant small fragments dispersed in distilled water were filtered through a 0.22 $\mu$m filter to isolate the NPs.

**2.3. Design of the 3D Printed PLA Scaffolds.** The original PLA scaffolds were designed using SolidWorks 2019−2020 software and were characterized by a hexagonal honeycomb 8 mm in height, 15 mm in width, and 30 mm in length with a rectangular pore sized at 850 $\mu$m. The rectangular pore structure was designed and printed as reported previously.[23] Smaller 3D PLA scaffold wafers, having a dimension of 5.85 mm diameter and 1 mm height, exactly fit inside the well of a 96-well plate and were also designed using SolidWorks. A FlashForge Creator Max Dual Extruder 3D Printer (Manufacturer-FlashForge USA) was used for all the 3D printing processes. 3D printing was done using 1.75 mm PLA filaments. The temperature for printing was set to 200 °C, and the printing bed was set at 50 °C. A printing speed of 60 mm/s was used for the printing process, and the postprocess scaffold was removed from the 3D printer and allowed to cool at room temperature.

**2.4. Application of the PER Process on 3D Printed PLA Scaffolds.** The PER process was carried out on the surface of different 3D PLA scaffolds (honeycomb pore-shaped, rectangular pore-shaped, and small 96-well culture plate fitting designs) like the hydrophobic surgical masks described in the previous section. To optimize $AgNO_3$ concentrations, the smaller 96-well plate-sized 3D scaffolds were used. Wafers were immersed in different concentrations of $AgNO_3$ ranging from 3.1 $\mu$M to 250 mM before undergoing the PER process as described for the larger scaffolds.

Removal of loosely attached NPs was performed using either sonication, a medium soak, or a sequential treatment of both. In brief, AgNP-/AuNP-modified scaffolds were added to 5 mL of a phosphate-buffered saline (PBS) solution (pH 7.4) and sonicated using a bath sonicator (Fischer Scientific, model number-FS20) for 2 min to remove any unstable AgNPs attached on the surface. The medium


https://doi.org/10.1021/acsami.2c01195
ACS Appl. Mater. Interfaces XXXX, XXX, XXX−XXX

soak consisted of wafers immersed in cell culture media (minimum essential medium Eagle (1×) with Earle's salts without L-glutamine and phenol red, manufactured by Corning) for 2 days. The sequential process included an initial 2 min sonication, followed by a 2 day medium soak. The treated NP disks were then cultured with either human fibroblast cells or bacteria.

**2.5. Characterizations.** X-ray photoelectron spectroscopy (XPS) was employed to elucidate the surface reduction process taking place on the substrates. XPS spectra of plasma-treated samples were obtained using a Phi 5000 VersaProbe made by Phi Electronics, Inc. (Chanhassen, WI USA). The X-ray source of this instrument is a monochromatic, focused, Al K-alpha source ($E$ = 1486.6 eV) at 25 W with a 100 $\mu$m spot size. The high-resolution XPS scans (average of 8 scans per analysis) were obtained with a pass energy of 23.5 eV and a step size of 0.1 eV.

The surface evaluation of the cellulose fibers, surgical masks, and 3D printed scaffold samples was done using scanning electron microscopy (SEM). Samples were sputter-coated with Au−Pd and observed using a field emission SEM (Quanta FEG 650 from FEI, Hillsboro, OR). Images were taken at different magnifications. The surface features and nanoscale roughness of surgical masks and 3D printed PLA scaffolds were systematically studied using 3D laser scanning confocal microscope VK-X1000 (developed by Keyence Corporation of America) with nanometer-resolution capabilities. Detailed surface analysis 3D surface imaging and a corresponding nanoroughness evaluation including a material ratio curve, arithmetical mean surface height ($S_a$), and developed interfacial area ratio ($S_{dr}$) were measured using the software developed by the Keyence Corporation of America. Transmission electron microscopy (TEM) imaging of the metallic NPs was carried out using a Tecnai Spirit T12 TEM (Thermo Fisher, formerly FEI) with an operating voltage range of 20−120 kV.

**2.6. Quantification of Silver Ion Release from AgNP-Modified 3D Scaffolds.** The quantification of silver ions released from the AgNP-modified 3D scaffolds was carried out using inductively coupled plasma mass spectrometry (Agilent Technologies 7700 ICP−MS, Santa Clara, CA). Agilent Technologies Mass Hunter software (v4.3) was used for data acquisition and analyses. Different batches of AgNP-modified 3D scaffolds such as 25, 12.5, 6.2, and 3.1 mM AgNPs (all with the same dimensions) were incubated with 10 mL of pH 7.4 PBS. These 3D scaffolds immersed in PBS were then placed in an incubator and agitated at a speed of 120 rpm at 37 °C. For the quantification purpose, 1 mL of the supernatant from each of the samples was extracted and diluted with 9 mL using a mixture of 1:3 molar ratio of nitric acid and hydrochloric acid for the ICP−MS analysis. For the time-dependent release profile quantification, 3.1 mM AgNP-modified 3D scaffolds were incubated in 10 mL of PBS for different time periods such as 1, 3, 5, and 7 days. At each of the respective time points, 1 mL of the supernatant was extracted from different samples and diluted with 9 mL using a mixture of 1:3 molar ratio of nitric acid and hydrochloric acid for the ICP−MS analysis.

**2.7. Cytocompatibility and Cell Viability Assay.** A human cell model was used to explore cytocompatibility using the MTT (3-(4,5-dimethylthiazol-2-yl)-2,5-diphenyltetrazolium bromide) assay to test overall cell viability in the presence of AgNP-coated PLA samples. The cell model known as NHLF purchased from Lonza is a normal human lung fibroblast cell line, which was selected and subsequently used in the cytocompatibility studies. The cells were incubated in a Falcon 96-well plate along with the aforementioned PLA scaffolds designed to fit in each well. The MTT assay reagents were purchased as a kit from Thermo Fisher as "CyQUANT MTT cell proliferation assay kit", catalogue number V13154. The protocol used to perform the assay (cell viability test) was provided by the manufacturer (publication number: MAN0019028). The "complete assay protocol" was chosen from the two options listed in the manufacturer's instructions. The cells were counted using a Bio-Rad TC-20 Automated Cell Counter. Cells were plated onto the samples at a density of 30,000 cells/100 $\mu$L for every well in a 96-well plate. After a period of 48 h of incubation, the plate was read at an absorbance of 570 nm as per the manufacturer's protocol.

**2.8. Antibacterial Studies of Face Masks and 3D Printed Scaffolds Modified with AgNPs.** M1 and M3 (outer and inner) layers of the surgical mask which had been coated with a AgNP coating were provided, along with controls, for antimicrobial testing. From each layer and its corresponding treatment, at least fifteen 24 mm diameter disks were measured and cut. These disks were then autoclaved and allowed to cool before testing. Five bacterial strains which represent some of the most influential pathogens to threaten patient health, primarily as medical device colonizers or through postoperative infections (specifically in joint repair and replacement), were selected. These included *Escherichia coli* K-12 strain MG1655 (denoted as JJM5) from Dr. J. Jeffrey Morris's culture collection, *Pseudomonas aeruginosa* strain PA01 (denoted as PA01) gifted by Dr. Asim Bej, UAB Biology, *P. aeruginosa* strain PA14 (denoted as PA14) gifted from Dr. William Swords, UAB Department of Medicine. Both 6726 and 9023 are clinical strains gifted by Dr. William Benjamin, UAB Hospital Department of Pathology. 9023 is a methicillin-resistant *Staphylococcus aureus* culture, and 6726 is a *S. aureus* culture.

Each of these strains was revived from a frozen culture preserved at −80 °C. In brief, each specimen was thawed at room temperature, gently vortexed, and then aseptically plated for isolation with a four-quadrant streak. Plates were incubated overnight at 37 °C. A single isolated colony was transferred using a 10 $\mu$L loop to a Lenski flask containing 10 mL of Luria−Bertani (LB) broth and again incubated overnight at 37 °C under agitation at 120 rpm. Optical density readings were evaluated using a BioTek Synergy H1 microplate reader at 600 nm ($OD_{600}$). Readings were used to normalize bacterial concentrations to $5 \times 10^8$ cfu/mL in the soft agar overlays. Once the overlays were hardened, disk diffusion studies for each mask layer and its respective treatment (AgNPs or control) were plated in triplicate and incubated at 37 °C overnight. The diameter of inhibition (DOI) around each disc was then measured using a clear plastic ruler through the center of the disc to the largest diameter and recorded in millimeters. If there was no zone of inhibition around the disc, the DOI measurement was recorded as zero.

Inhibitory concentration testing was used to assess AgNP-coated scaffolds for antimicrobial efficacy. For this testing, one Gram-positive bacteria (methicillin-resistance *S. aureus* strain 9023) and one Gram-negative bacteria (*P. aeruginosa* strain PA14) were used. Both strains have demonstrated high-affinity infection rates in postoperative joint replacement. In brief, 100 $\mu$L of an overnight culture was transferred into 9.9 mL of LB broth and placed in an incubator shaker at 37 °C and 120 rpm for 4 h to produce an exponential culture. Optical density readings were taken of both cultures before normalizing each culture to $1 \times 10^8$ cfu/mL. Serial dilutions were then performed to $10^5$ in normal saline using sterile Falcon tubes.

Three $AgNO_3$ concentrations, including the 12.5, 6.25, and 3.12 mM $AgNO_3$ concentrations, with the lowest cytotoxicity (based upon the data obtained from the MTT assay) were tested. In addition to these NP treatments, two types of control PLA scaffolds were run: a PLA control scaffold and a PLA control scaffold subjected to hydrogen plasma treatment, which had also been sonicated and soaked in the medium. Four replicates of each scaffold type were incubated for each bacterial strain. In short, a single scaffold was placed in its own well on a 96-well microtiter plate. This was repeated to a total of four replicates for each treatment or control. The controls were separated from the treatments by a row of LB media, and bacterial species were separated by two rows of LB media to prevent cross-contamination. 100 $\mu$L aliquots of LB media were pipetted into all wells with a scaffold using a multichannel pipette. A 100 $\mu$L aliquot of the $1 \times 10^5$ bacterial dilution was then inoculated into each well for the set of scaffolds for PA14. The same was repeated for the scaffolds testing 9023 (reference Table S10 in the Supporting Information to see the plate layout). A lid was placed on the plate, and the plate was then incubated overnight in a shaker incubator at 37 °C at 80 rpm for 18 h.

Once the incubation was complete, the scaffolds were removed from the microtiter plate using aseptic techniques. The remaining planktonic fractions were serially diluted to $10^{-11}$, and then 5 $\mu$L was spot-titered sequentially onto the LB agar plates. The plates were


https://doi.org/10.1021/acsami.2c01195
ACS Appl. Mater. Interfaces XXXX, XXX, XXX−XXX

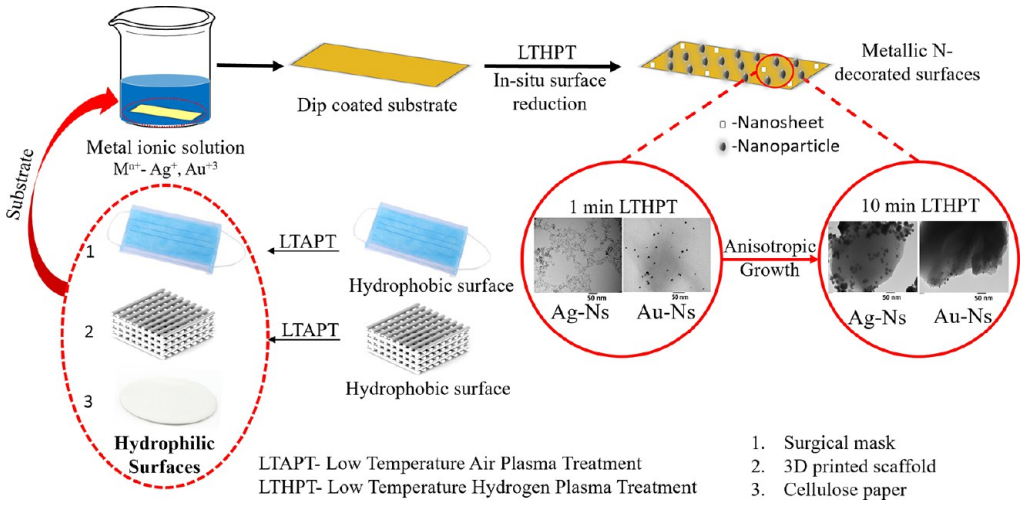


**Figure 1.** Schematic representation of the *in situ* PER process on hydrophilic and hydrophobic polymeric substrate materials and subsequent time-dependent formation of gold and silver nanostructures (AuNPs and AgNPs).

placed in a 37 °C incubator overnight. Upon removal the next morning, colony counts were performed, and the plates were photographed. The images were imported into preview on Mac, and a grid was overlaid on the image where the spots for each series of titers should be. These grids were then cropped from each of their respective images and pasted together to form one continuous dilution series for the ease of visual assessment. The original images of the plates are available upon request.

**2.9. Statistical Analysis.** Statistical analysis was performed using R Studio (please see Figure S18 in the Supporting Information for more detailed information on the script). DOI measurements were evaluated with a fitted general linear model using a $\gamma$ distribution. The best model was selected using aictab in the AICcmodavg package. Model parameters included only bacteria. Pairwise performance comparisons of AgNP activity between bacterial species were then elucidated using the fit glm model and emmeans analysis from the data collected in the preliminary experiments. *P*-Value adjustments for multiple comparisons were made using the Tukey method. Control DOI measurements were all zero, creating a bimodal break in the data, so these were removed from the analysis.

## 3. RESULTS AND DISCUSSION

The PER process is schematically represented as shown in Figure 1. This PER process can be carried out on a hydrophilic polymer substrate such as cellulose paper by direct low-temperature hydrogen plasma treatment (LTHPT). In the case of hydrophobic polymer substrates such as PP-based fibrous surgical masks and PLA 3D printed scaffolds, they must first be pretreated with low-temperature air plasma treatment (LTAPT) for imparting hydrophilicity. This LTAPT treatment can drastically improve the surface wettability of hydrophobic polymeric substrates, which makes them hydrophilic. Subsequently, these three different substrates with hydrophilic nature can be simply dip-coated with different metal ionic solutions of gold and silver ($Ag^+$ and $Au^{3+}$), followed by subjecting them to LTHPT for accomplishing the PER process. Finally, this PER process modifies the surface of all these substrates with metallic nanostructures, which clearly suggests that this process is both substrate- and surface- (whether hydrophobic or hydrophilic) independent.

**3.1. Proof of Concept of the PER Process on a Hydrophilic Cellulose Paper.** Proof of concept of this method was first demonstrated on a hydrophilic cellulose paper. The cellulose paper was dip-coated with gold and silver salts (Figure S1a) and then subjected to LTHPT for 10 min (Figure S1b,c). Surface reduction is evident from the color changes of the treated cellulose papers to black and purple for silver and gold, respectively (Figure S1d). XPS was utilized to systematically study the surface reduction process taking place on the surface of cellulose papers.

The control cellulose paper exhibited elemental carbon and oxygen at the surface. In the case of unmodified silver salt dip-coated cellulose paper, the surface atomic percentage of silver was 2.1% (Figure S2), whereas with the hydrogen plasma surface reduction, this number jumped to 25.9%. The PER is directly responsible for this, first increasing NP nucleation, followed by the NP's growth on the paper. Furthermore, the oxidation state of silver on the surface was recorded. The high-resolution silver spectrum of plasma-treated cellulose paper exhibited two peaks at 369 and 375 eV, which correspond to $Ag^0$ $3d_{5/2}$ and $Ag^0$ $3d_{3/2}$, respectively (Figure S2). A binding energy difference of 6 eV between $Ag^0$ $3d_{5/2}$ and $Ag^0$ $3d_{3/2}$ is consistent with AgNP formation mechanistic reported in the literature,[18] clearly suggesting that PER was successful in reducing silver from a higher ($Ag^+$) to a lower oxidation state ($Ag^0$). This ionic shift primes the chemical environment to facilitate NP formation on the polymer surface. We performed the same systematic examination of the LTHPT gold-coated cellulose paper surfaces and observed the same trend of increase in the surface atomic percentage of gold on plasma-modified papers when compared to unmodified dip-coated papers (Figure S3). This observation also implies that the LTHPT reduced the gold metal salts into lower oxidation states, as observed with the silver samples. The high-resolution XPS spectrum of gold was used to verify the oxidation state changes after this process. In the case of gold, the high-resolution XPS spectrum exhibited four peaks at 85, 86.5, 89, and 91.5 eV. These peaks correspond to $Au^0$ $4f_{7/2}$, $Au^{3+}$ $4f_{7/2}$, $Au^0$ $4f_{5/2}$, and $Au^{3+}$ $4f_{5/2}$, respectively, (Figure S3) and suggest that mixed oxidation states (+3 and 0) were present on the surface. However, it is worth mentioning that the $Au^0$ $4f_{7/2}$ and $Au^0$ $4f_{5/2}$ peaks were more predominant in comparison with $Au^{3+}$ $4f_{7/2}$ and $Au^{3+}$ $4f_{5/2}$, providing evidence for the surface reduction of gold into a lower oxidative state, circumstances again which provide an optimal environment for the formation of AuNPs. The observed high-resolution spectrum was


https://doi.org/10.1021/acsami.2c01195
ACS Appl. Mater. Interfaces XXXX, XXX, XXX−XXX

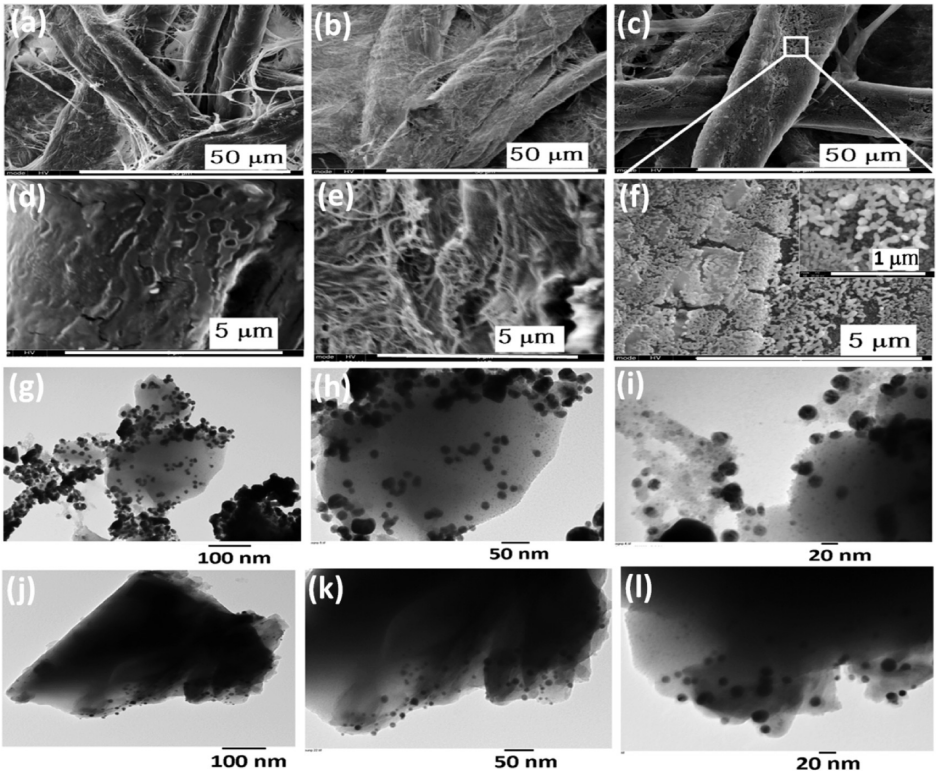


**Figure 2.** SEM images of control cellulose paper (a,d), cellulose paper dip-coated with gold(III) chloride after LTHPT (b,e), and cellulose paper dip-coated with silver nitrate after LTHPT (c,f). TEM images of the AgNPs formed on the surface of cellulose paper (g–i); TEM images of the AuNPs formed on the surface of cellulose paper (j–l).

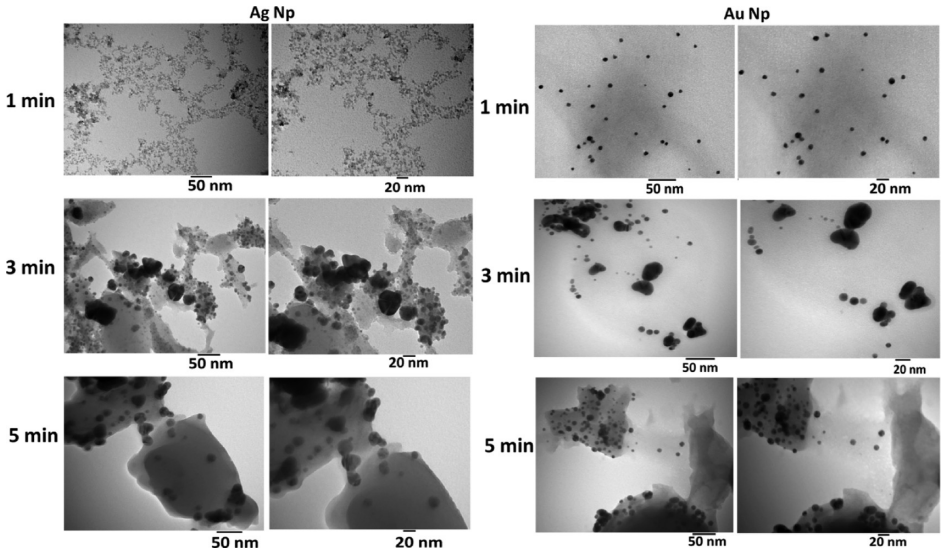


**Figure 3.** TEM images of AgNPs and AuNPs formed at 1, 3, and 5 min time points.

comparable to that of AuNPs synthesized via a laser ablation process.[19] Taken together, the XPS analysis establishes successful *in situ* application of this surface PER process on both Ag and Au on cellulose paper. To characterize the surface features of these reduced metals more thoroughly, we examined the silver- and gold-reduced papers under SEM. SEM imaging of control untreated cellulose paper showed fiber architecture with no evidence of nanostructuring on its surface (Figure 2a,d).

Interestingly, the PER process of silver ions on the paper's surface exhibited the formation of both NPs and nanosheets decorating the top of the fiber surface (Figure 2c,f). This observation supported our claim of surface reduction and subsequent formation of nanostructures on the top of cellulose paper. The gold ions formed a coating, but unlike silver, there were no distinct NPs observed (Figure 2b,e). This could be due to the diminutive size of the AuNPs formed or a result of all the distinct particles fusing into a thin layer. In order to test our suspicions, we extracted the gold and silver nanostructures formed on the cellulose paper and examined them by TEM. The TEM images of silver nanostructures from the cellulose paper treated for 10 min showed the formation of clustered 20


https://doi.org/10.1021/acsami.2c01195
ACS Appl. Mater. Interfaces XXXX, XXX, XXX–XXX

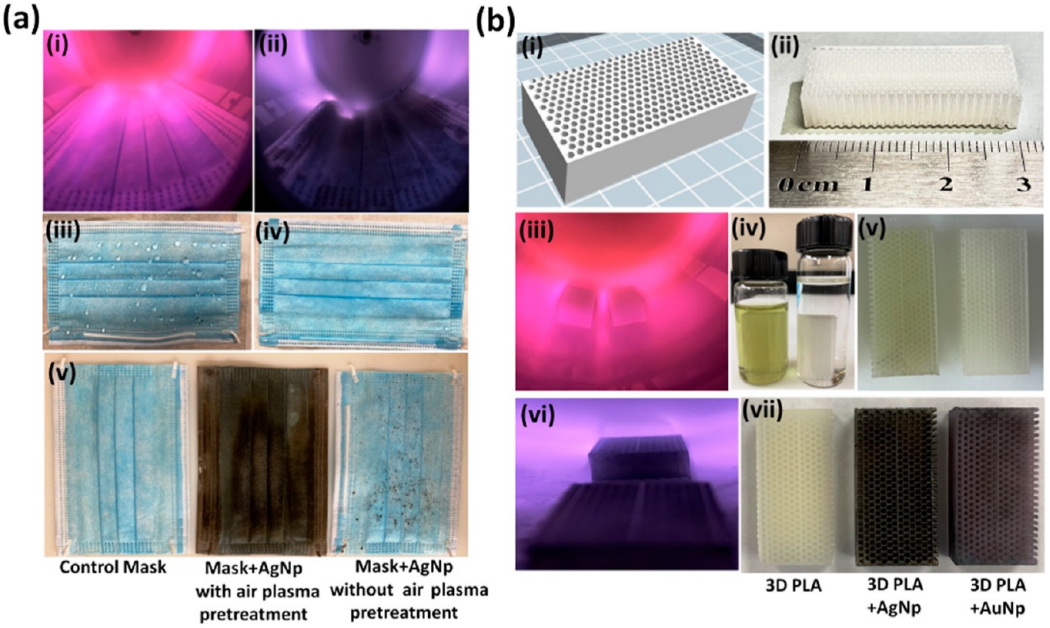


**Figure 4.** Images showing the PER process on the outer layer (M1) of a surgical mask (a) and 3D printed PLA scaffolds (b). (ai) M1 layer undergoing LTAPT, (aii) M1 layer dipped in silver nitrate undergoing LTHPT, (aiii) silver nitrate sprayed on the top of the M1 layer without LTAPT, (aiv) silver nitrate sprayed on the top of the M1 layer with LTAPT, and (av) image of untreated control and the LTHPT M1 layer. (bi,ii) Images of the untreated control 3D printed PLA scaffold, (biii) 3D scaffold undergoing LTAPT, (biv,v) 3D scaffolds dipped in silver nitrate and gold(III) chloride, (bvi) 3D scaffolds undergoing LTHPT, and (bvii) 3D scaffolds after surface reduction with LTHPT.

nm spherical AgNPs which were situated on top of a thin anisotropic 2D silver nanosheet composed of ultratiny AgNP clusters with a particle size of 2−3 nm (Figure 2g−i). The observed mixture of two-dimensional (2D) nanosheets and NPs was consistent with the SEM observations. We observed a similar formation of 2D nanosheets and NPs for the AuNPs as well. However, here the nanosheet formation was predominant with the presence of only a few AuNPs formed at the edge of the nanosheet (Figure 2j,l). The size of the AuNPs was ∼20 nm. The TEM findings inspired us to explore the time-dependent formation of the mixed nanostructures to unravel the mechanism involved.

Subsequently, we carried out additional surface reduction tests for both AuNPs and AgNPs at 1, 3, and 5 min time points on cellulose paper (Figure S4a−c). NPs from the surface of the cellulose paper at different time points distinctly exhibit a time-dependent formation mechanism. At 1 min, there are clear, distinct spherical NPs of both silver and gold (Figure 3). The anisotropic growth of these smaller NPs is evident by the growth in size and elongation seen at 3 min. Finally, at 5 min, they have fully developed into anisotropic 2D nanosheets accompanied by NPs because of their oxidation-state change.

The observed phenomenon was consistent with recently reported transition-metal oxide nanostructures, which also grew anisotropically into 2D nanosheets with NPs as intermediates.[20] Consequently, we can guide the anisotropic evolution of AuNPs and AgNPs into sheets by varying the exposure time using this PER method. Photochemical methods, including high-energy UV light and free radicals, are one of the most common methods of initiating anisotropic growth in 2D metallic nanomaterials.[21] Our process exploits hydrogen radicals in combination with UV light photons from hydrogen plasma to interact with the metallic ion precursors. We suspect that this mechanism could be responsible for the observed time-dependent formation of anisotropic 2D metallic nanostructures.

**3.2. Application of the PER Process on Hydrophobic Fibrous and 3D Printed Polymer Surfaces.** One of the major aims of this present work was to develop an efficient, green process which can modify the surfaces of different hydrophobic polymeric substrates such as fibrous and 3D scaffolds with metallic nanostructures. Building upon previous work, we began with a fibrous surgical face mask made of hydrophobic PP. The surgical mask has three layers, namely, an outer (M1), middle, and inner (M3) layer. We used the M1 layer for the plasma treatment and characterization studies. Due to the extreme hydrophobicity, it was challenging to uniformly coat the surface of each layer. To solve this issue, the surface of the surgical mask was pretreated using air plasma to make it hydrophilic (Figure 4ai). Previous reports demonstrated that air plasma treatments can enhance the surface wettability of different polymer surfaces such as polyethylene, PP, and polystyrene.[22] This wettability is essential for the formation of a uniform layer of metallic nanostructuring on the mask surface. To test this axiom, we utilized both low-temperature air plasma pretreated (LTAPT) and untreated control mask layers in our surface reduction process.

Our findings show that the nitrate ($AgNO_3$) solution sprayed on the untreated mask pooled on the mask's surface. The LTAPT-pretreated mask samples, however, exhibited an even application of the salt solution (Figure 4aiii,iv). These observation droplets provided convincing evidence that LTAPT improved the surface wettability of the M1 layer. Following the LTAPT, we dip-coated the M1 layer in silver and applied LTHPT, producing a very uniform black nanostructured coating on the surface (Figure 4aii,v). Conversely, the control M1 layer had a nonuniform silver coating. This observation supports our claim that our PER process can be successfully adapted to hydrophobic substrates


https://doi.org/10.1021/acsami.2c01195
ACS Appl. Mater. Interfaces XXXX, XXX, XXX−XXX

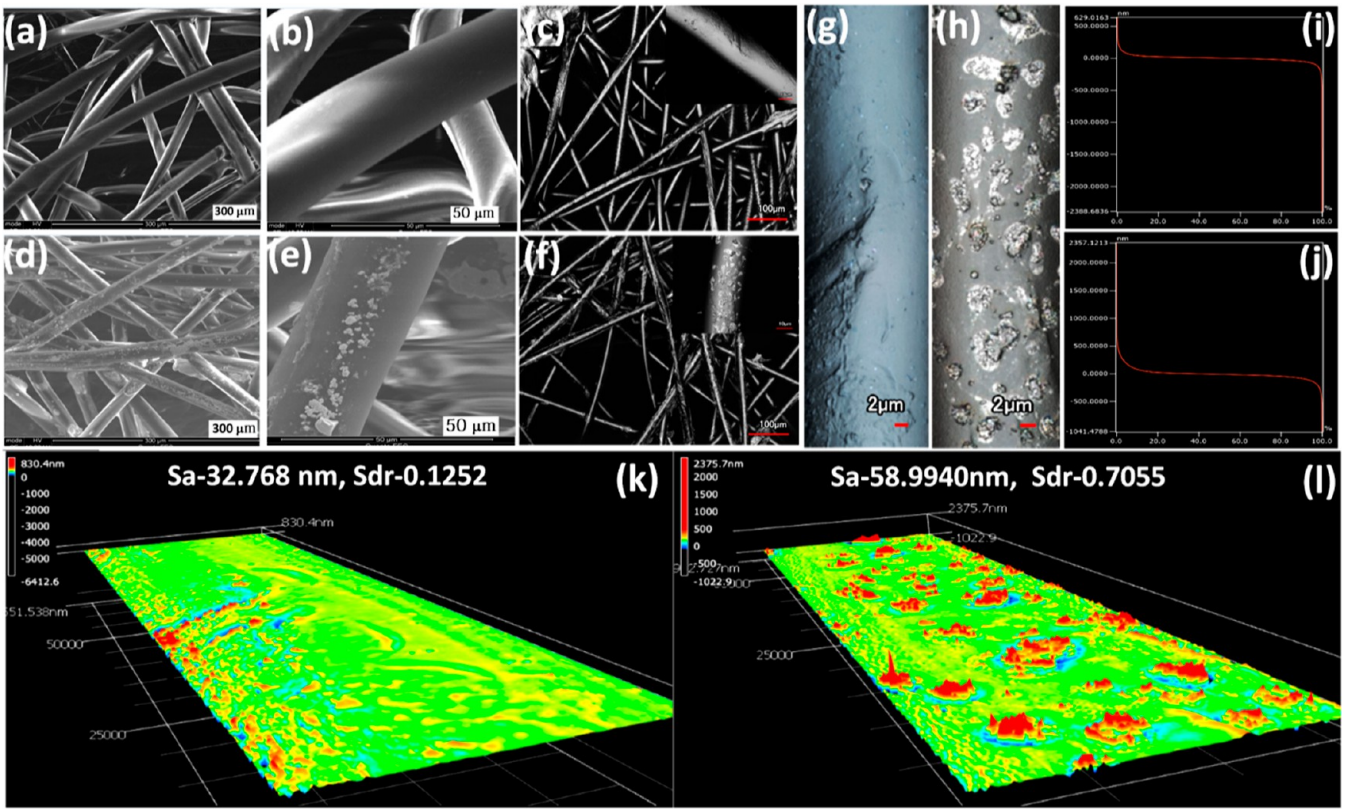


**Figure 5.** SEM imaging of the untreated surgical mask top layer (M1) (a,b) and LTHPT surgical mask top layer (M1) layer (d,e). 3D laser scanning confocal microscopy images of the untreated M1 layer (c) and images of the LTHPT M1 layer (f). Images of an individual fiber of the untreated M1 layer (g) and LTHPT individual fiber of the M1 layer (h). Material ratio curve of the untreated and LTHPT M1 layer (i,j). 3D surface image comparison of the untreated and LTHPT M1 layer (k,l).

by using a sequential combination of LTAPT and LTHPT. XPS analysis was used to quantify the surface atomic percentage difference between the two sides of the surgical mask, and the outer layer revealed a higher atomic percentage of silver (23%) on M1 in comparison with M3 having 8% M1 (mask's upper portion) and the inner layer M3 (mask's lower portion) (Figure S5). This difference in the percentage of deposition can be attributed to greater contact of the outer layer of the surgical mask to plasma exposure in comparison with the bottom inner layer M3. To demonstrate the versatility of this PER process, we then attempted the same sequential treatment on hydrophobic 3D polymer scaffolds using hydrophobic 3D printed honeycomb-shaped PLA scaffolds (Figure 4bi,ii). Similar to the mask sample, the PLA 3D scaffolds were first pretreated with LTAPT and then dip-coated in either Au or Ag metal ion solutions (Figure 4biii–v). Surface-reduced 3D scaffolds produced visual color changes unlike their dip-coated control counterparts (Figure 4vi–vii). SEM and 3D laser scanning confocal microscopy were used to obtain detailed information about the AgNP-modified mask samples. SEM images of the AgNP-modified mask surface exhibited the formation of large clusters of AgNPs on the fiber surface, which was clearly absent on the control fiber surface (Figure 5a,b,d,e).

The 3D laser scanning confocal microscopy surface images further revealed detailed information on the silver nanostructures on the mask fiber surface. The surface images demonstrate clusters of AgNPs on treated fiber surfaces, which were absent on the control fiber surface (Figure 5c,f). To better describe the nanostructuring observed, we imaged a single fiber from both the control and a treated fiber. Once again, we clearly observed the formation of both distinct NPs and large clusters of NPs, which a formed sheet-like network on the fiber surface. This nanostructuring was completely absent on the control fiber surface (Figure 5g,h).

The observation of anisotropic silver nanosheets on the mask surface mimics the findings from our hydrophilic cellulose paper surface experiments. Furthermore, we evaluated the effect of this nanostructuring on the surface roughness profile of the mask fibers. The material ratio curve and 3D surface images of the AgNP-decorated fibers were different than those of the control fibers (Figure 5i–l). More specifically, the arithmetical mean surface height ($S_a$) and developed interfacial area ratio ($S_{dr}$) of AgNP-modified mask surfaces were higher than those of the untreated control mask. This suggests that the AgNP surface modification process resulted in an increased nanoscale surface roughness and surface area compared to their control counterparts.

Furthermore, we have evaluated the formation of AgNPs and AuNPs formed on the surface of 3D printed scaffolds. SEM images of AgNP-modified 3D scaffolds exhibited the formation of distinct sheets. The higher-magnification image shows the formation of distinct AgNPs on the surface of this sheet (Figure S6). This observed formation of both 2D nanosheets and distinct NPs of silver nanostructures mirrors both our surgical face mask and cellulose paper surfaces. In the case of AuNP-modified 3D scaffolds, they exhibited small clusters of AuNPs on the surface (Figure S6). This authenticates the ability of our surface reduction process to efficiently modify 3D printed scaffold surfaces with both


https://doi.org/10.1021/acsami.2c01195
ACS Appl. Mater. Interfaces XXXX, XXX, XXX−XXX

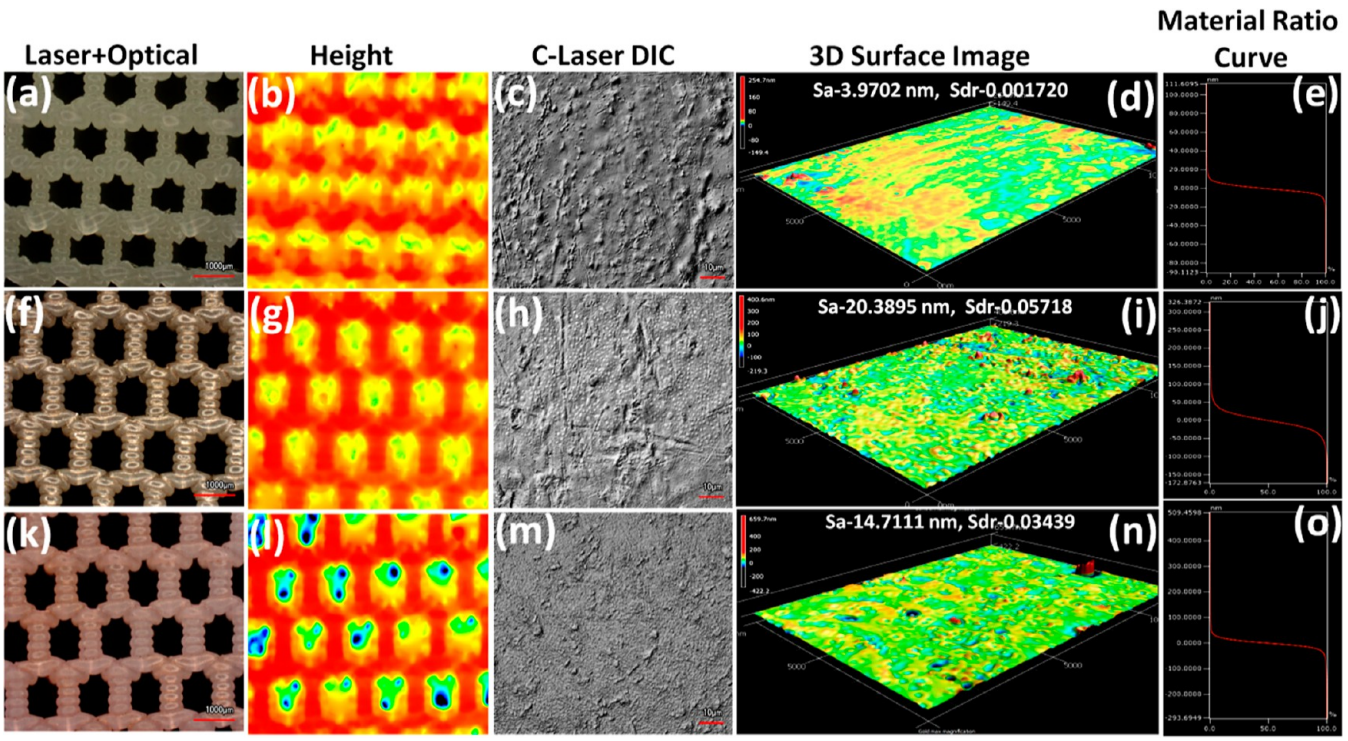


**Figure 6.** 3D laser scanning confocal microscopy images of control 3D printed honeycomb-shaped PLA scaffolds (a–e), 3D printed honeycomb-shaped PLA scaffolds AgNPs (f–j), and 3D printed honeycomb-shaped PLA scaffold AuNPs (k–o).

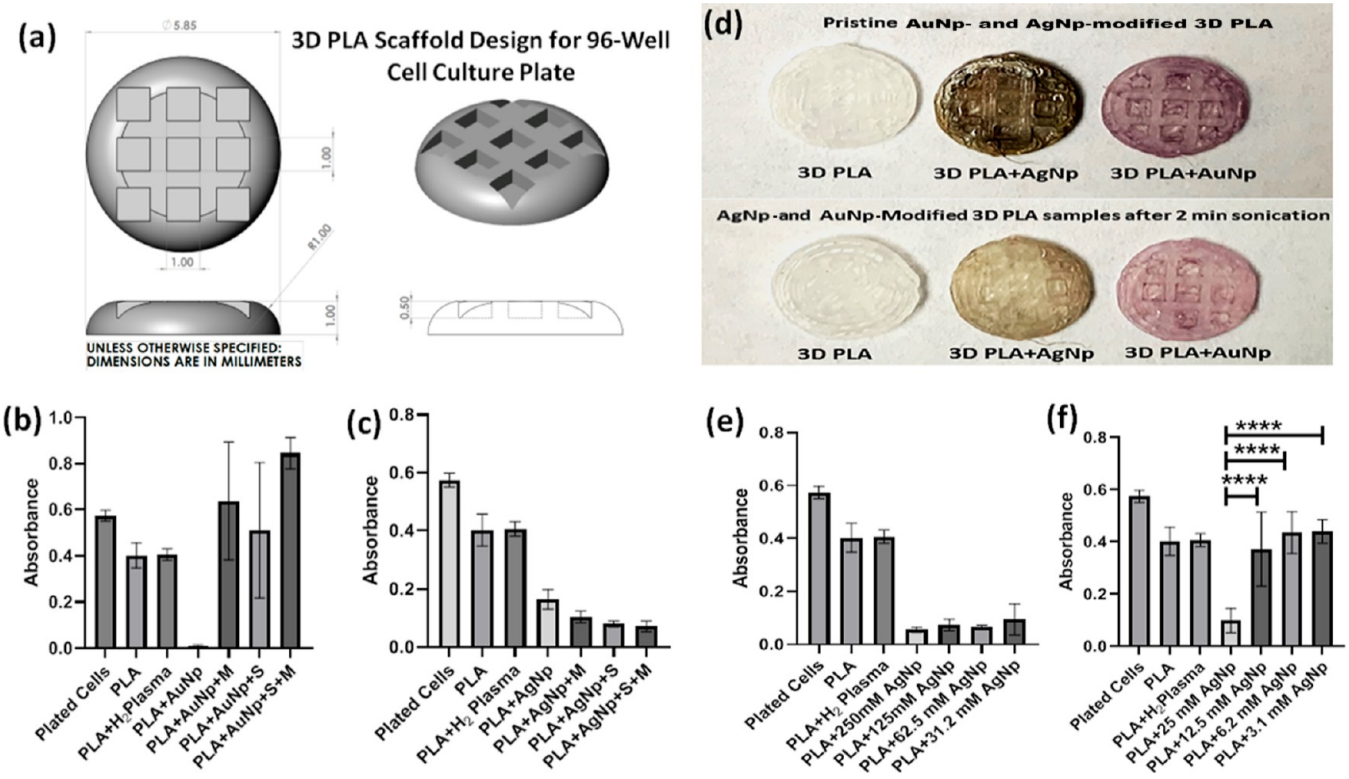


**Figure 7.** Computer-aided design image of the 3D PLA scaffold fitting the well of a 96-well cell culture plate (a), MTT assay of AuNP-modified 3D scaffolds with and without different postprocessing methods such as sonication and medium soaking (b), AgNP-modified 3D scaffolds with and without different postprocessing methods such as sonication and medium soaking (c), images of the 3D PLA scaffolds before and after sonication wash (d), and AgNP-modified scaffolds prepared from various concentrations of silver nitrate solution (e,f). The symbol M indicates the medium-soaked scaffolds, and the symbol S indicates the sonicated scaffolds.


https://doi.org/10.1021/acsami.2c01195
ACS Appl. Mater. Interfaces XXXX, XXX, XXX–XXX

AgNPs and AuNPs. 3D confocal laser scanning microscopy surface measurements provided further insight on nanostructuring on the surface of these 3D scaffolds.

It was revealed that both AgNP- and AuNP-modified 3D scaffolds have a higher arithmetical mean surface height ($S_a$) and developed interfacial area ratio ($S_{dr}$) when compared with those of control scaffolds (Figure 6). This again demonstrated that both AgNP and AuNP surface modification processes resulted in an increase in nanosurface roughness and surface area. This observed metallic nanostructuring of AgNPs and AuNPs on 3D scaffolds of the PLA surface may potentially benefit tissue engineering applications such as bone−tissue engineering. Altogether, these results support our claim of efficient metallic nanostructuring on different hydrophobic polymer surfaces such as fibrous and 3D printed polymer scaffolds using this PER process.

Modifying 3D scaffolds in a uniform manner can be quite challenging and can oftentimes require robust optimization. The honeycomb PLA designs which were previously used for the initial characterization studies were simple and only contained unidirectional pores that did not serve specific purposes. Therefore, to better test the capability of the PER process to uniformly modify the surface of a 3D scaffold, we manufactured a more complex 3D printed PLA scaffold that has a rectangular pore geometry.[23] SEM images showing the top and cross-sectional areas were taken for the AgNP- and AuNP-modified scaffolds. The SEM images confirmed the presence of AgNPs on both the top and cross-sectional areas of the cut scaffold (Figure S7). Energy-dispersive X-ray spectroscopy (EDAX) mapping of the cross-sectional area further supported the SEM images, where one can clearly observe the distribution of AgNPs (Figure S8). The AuNP-modified scaffold also has a similar presence of NPs at both top and the cross-sectional area of the scaffold (Figures S9 and 10). Even though the extent of modification was not identical for both the top and cross-sectional surfaces, the scaffolds still exhibited an appreciable amount of modification on the cross-sectional area. This demonstrates the capability of the PER process to efficiently nanostructure the 3D scaffolds. However, we do acknowledge the fact that complete homogeneous modification of more complex 3D scaffolds cannot be accomplished using the present method. This is because plasma generated inside the chamber under low pressure cannot completely diffuse efficiently inside the pores, which may lead to inhomogeneous/gradient modification of complex 3D scaffolds. The solution for this problem is to use an atmospheric-pressure plasma jet (APPJ), where plasma can be generated at room temperature in the form of a jet, which could be applied to any complex 3D printed materials to homogeneously modify the surface.[24] Hence, in our future studies, we plan to extend our low-pressure PER process to APPJ, where the surface of more complex 3D printed scaffolds can be functionalized more uniformly.

**3.3. Cytotoxic and Antimicrobial Evaluation of Metallic Nanostructure-Modified 3D Printed Polymer Scaffolds and Face Masks.** Cytotoxicity is a common challenge when incorporating metallic NPs in biomedical materials. Hence, it is essential to test the cytocompatibility of the metallic nanostructure produced after the PER process. To systematically evaluate this cytocompatibility, we first 3D printed small PLA scaffold wafers (5.85 mm diameter; 1 mm height) that exactly fit the size of a 96-well plate (Figure 7a). The objective of printing such a small-sized 3D scaffold was to ensure more reliable and robust in vitro testing of the metallic NP-modified 3D scaffolds. The surface of the 3D scaffolds was then subjected to the PER process for modification with both AgNPs and AuNPs. Subsequently, we used the MTT assay to calculate the viability of the cells treated with these nanostructured scaffolds. Initial MTT data obtained demonstrated a significant reduction in the cell viability for both AgNP- and AuNP-modified 3D scaffolds (Figure 7b,c).

This drove the refinement of our process to mitigate loosely attached NPs from scaffold surfaces via two different strategies: (1) a 2 min sonication to remove the unreacted metallic salt precursors and unstably anchored metallic NPs and (2) a 2 day medium soaking to improve its cytocompatibility. With regards to the medium soaking process, we anticipated similar removal of unreacted metallic salt precursors and unstably anchored particles. To directly visualize the impact of sonication washing, immediately after the PER process, both AuNP- and AgNP-modified scaffolds were sonicated for 2 min. After the sonication process, there was a noticeable reduction in the color intensity of both AgNP- and AuNP-modified scaffolds (Figure 7d). This clearly demonstrates the efficacy of adding a sonication wash step to remove any present unstably anchored particles from the surface. The observed cytotoxic response of the pristine AgNP- and AuNP-modified 3D scaffolds could be due to the rapid release of the unstably anchored AgNPs and AuNPs from the 3D scaffolds. This proved to be an interesting observation, which leads us to believe that a gentle sonication process could have a profound impact on removing the excess/unstable NPs that would otherwise decrease the overall cytocompatibility. We then proceeded to systematically test the cytocompatibility of the processed 3D printed scaffolds first with only sonication, then only cell medium soaking, and finally with a combination of sonication and medium soaking via the MTT assay. In the case of AuNPs, both these strategies were successful in terms of enhancing the cell viability (Figure 7b). Also, it was found that when we combined both these strategies, that is, a combination of sonication and medium soaking of the 3D scaffolds, it synergistically contributed to the enhancement of the viability of the cells. Thus, it was very clear that our combined postprocessing strategy was very successful in enhancing the cytocompatibility of the AuNP-modified 3D scaffolds. The observed improved viability of the cells may be attributed to the removal of the unreacted gold salt precursors and unstably anchored particles after the sonication or medium incubation process.

However, with the AgNP-modified 3D scaffolds, this combination strategy was not found to be effective in improving the cytocompatibility (Figure 7c). This realization inspired us to explore the concentration optimization of $AgNO_3$. Therefore, we varied the concentration of the $AgNO_3$ (ranging from 31.2 to 250 mM) used for the PER process. The resulting AgNPs produced from each specific concentration of $AgNO_3$ were named along with the concentration of $AgNO_3$ (e.g., AgNPs produced from 250 mM $AgNO_3$ were named 250 mM or 0.25 M AgNPs and so on) after the PER process, the scaffolds were sonicated and incubated in the medium as mentioned earlier. However, it should be noted that this strategy also did not aid in improving the cell viability but rather was mostly done to ensure consistency within the process (Figure 7e). Finally, we decided to repeat the experiment using a concentration range, which was 10-fold lower than the aforementioned concentrations (specifically ranging from 25 to 3.12 mM). After the PER process, these


https://doi.org/10.1021/acsami.2c01195
ACS Appl. Mater. Interfaces XXXX, XXX, XXX−XXX

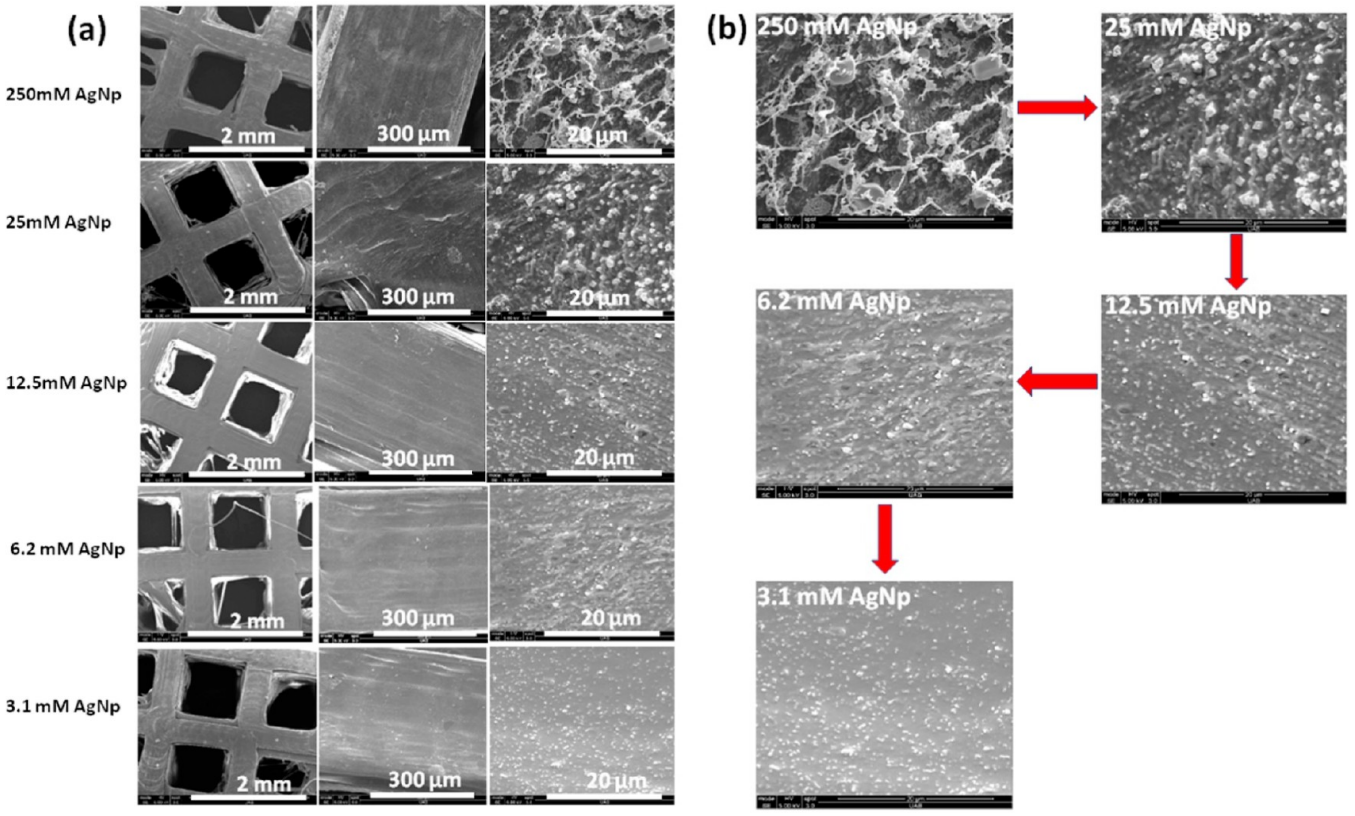


**Figure 8.** SEM images of the 3D printed PLA scaffolds modified with AgNPs prepared using different concentrations of silver nitrate (a) (images from left to right in each row represent different magnifications). Flow diagram showing the transition of the morphology and distribution of AgNPs at different concentrations (b) (representative SEM images shown in the flow diagram were all taken at the same magnification and settings).

scaffolds were then subjected to sonication and medium soaking. The dark color of these AgNP-modified scaffolds clearly became lighter after the sonication process, which indicates that this process helps to remove the unstably anchored AgNPs from the surface of 3D scaffolds (Figure S11). The MTT assay results have clearly shown a very significant increase in the viability of the AgNP-modified scaffolds for the lowest-concentration batches, more specifically, 12.5, 6.2, and 3.1 mM AgNPs (Figure 7f). These data suggest that the cytotoxic response of the AgNPs formed on the surface of the 3D scaffold after the PER process was directly proportional to the concentration of $AgNO_3$. These data clearly show that our optimizations improve upon the cytocompatibility of both AgNP- and AuNP-modified scaffolds using this PER process. These results have proven the beneficial addition of our postprocessing strategy to increase the safety of NP-coated biomedical implants and can be applied for broader medical applications.

The SEM imaging and EDAX mapping were utilized to perform more detailed evaluations, which would allow us to observe any differences in the distribution of AgNPs formed on the surface of 3D scaffolds with varying concentrations of $AgNO_3$.

SEM imaging of the 250 mM AgNPs showed anisotropic growth of AgNPs with a mixture of small sheets and large clusters of particles, which joined as nanowires. This nonuniform and high concentration of AgNPs may be responsible for the observed cytotoxic behavior of 250 mM AgNPs. Furthermore, the 10-fold diluted concentration batch (25 mM AgNPs) showed a comparatively smaller number of NPs and sheets with more uniformity (Figure 8). This further corroborated our hypothesis that any observed NP deposition was reliant on the concentration-dependent formation of AgNPs. Subsequently, while imaging the lowest-concentration samples (12.5, 6.2, and 3.12 mM AgNPs), we noticed that as the concentration decreased, the anisotropic growth of AgNPs became less predominant, while their uniformity noticeably increased. This would most likely be the reason for the increased cytocompatibility of these lowest-concentration batches of AgNPs. More importantly, in the 3.12 mM AgNPs, the particles were found to be more uniform and stably anchored on the surface of the 3D scaffolds. The EDAX mapping images of all these different lower concentrations of the AgNP-modified scaffolds further confirmed the same trend of more uniform and less concentrated AgNP modification of 3D scaffolds (Figures S12−S16). Furthermore, we made use of inductively coupled plasma mass spectrometry (ICP−MS) analysis to quantify the silver ions released from the AgNP-modified 3D scaffolds. Different concentrations of the AgNP (25, 12, 6.2, and 3.12 mM AgNPs)-modified 3D scaffolds were incubated in PBS solution, and quantification was performed using ICP−MS analysis (Figure S17). Interestingly, all samples exhibited a small 5 ppb release of silver ions, regardless of the concentration. Furthermore, we tested the release profile of 3.12 mM AgNPs at different time periods such as 1, 3, 5, and 7. A similar release profile of around 5 ppb was observed independent of time. These observations clearly suggest the stable anchoring of the lowest-concentration batches of AgNPs on the surface 3D scaffolds mitigate the likelihood of a significant number of NPs from releasing into the surrounding


https://doi.org/10.1021/acsami.2c01195
ACS Appl. Mater. Interfaces XXXX, XXX, XXX−XXX

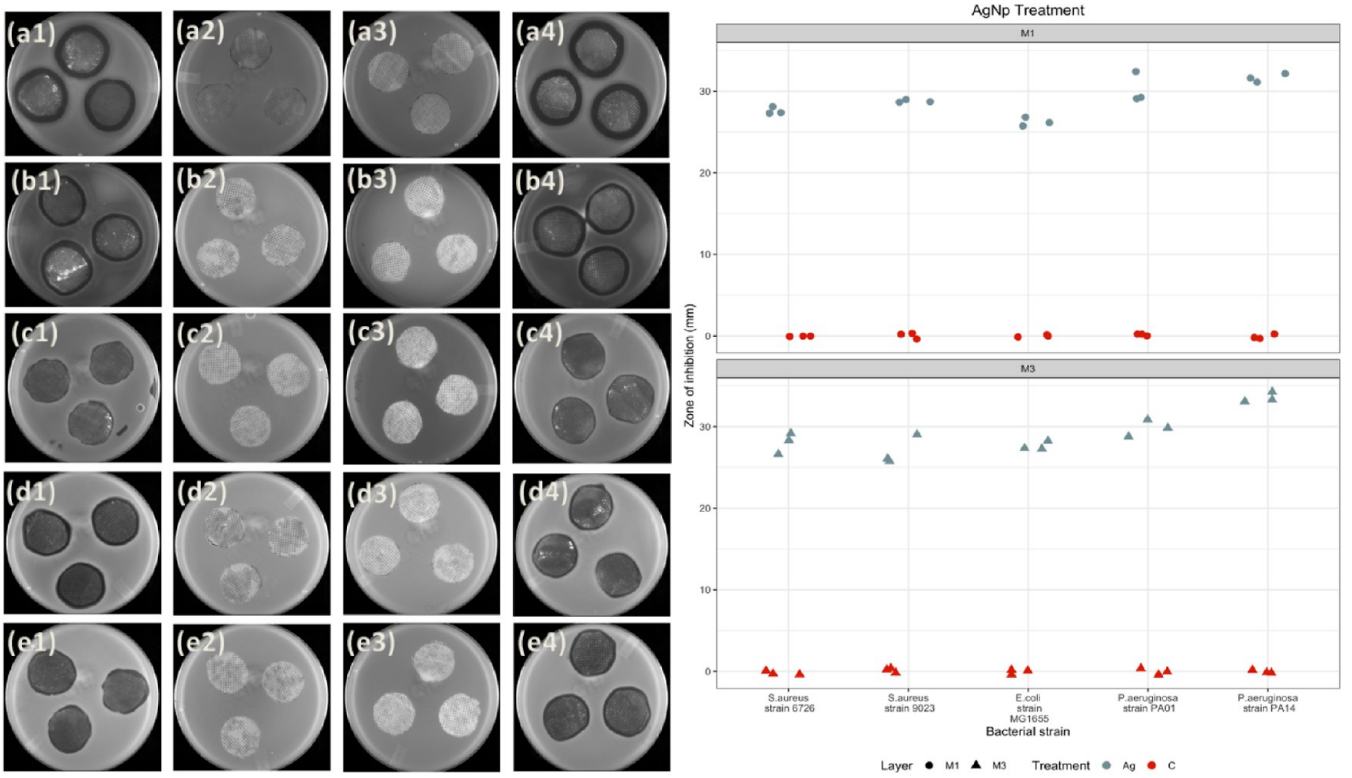


**Figure 9.** DOI measurements for the AgNP coating. The top graph is the outer mask (M1) layer and corresponds to images a1−e1. The bottom graph is the inner mask (M3) layer and corresponds to images a4−e4. Rows a−e represent different strains. Row a: *P. aeruginosa* strain PA01, row b: *P. aeruginosa* strain PA14, row c: *E. coli* strain MG1655, row d: resistant MRSA strain 9023, and row e: *S. aureus* strain 6726. Columns represent the mask layer and its treatment. Column 1: outer mask layer (M1)-AgNP-treated, column 2: outer mask layer-control, column 3: inner mask layer (M3)-control, and column 4: inner mask layer (M3)-AgNP-treated.

environment. Thus, it was very clear that lowering the concentration of $AgNO_3$ and subjecting the scaffolds through the postprocessing of sonication and medium soaking further improve this PER process' cytocompatibility.

A microbiological assessment of the antibacterial properties of the AgNP-modified surgical mask samples was conducted using disk diffusion and inhibitory concentration studies (Figure 9).[25] Five bacterial strains were selected, which represented some of the most common pathogens threatening patient health, primarily as medical device colonizers or through postoperative infections (specifically in joint repair and replacement).[26] For the disk diffusion studies, raw measurement diameters and their respective means for the M1 and M3 layers are given in Tables S1 and S2.

The average DOI across all bacteria (for both mask layers) was 29 mm. The mean DOIs for each bacterial species (M1 + M3 combined) were as follows: 30 mm for PA01, 32.5 mm for PA14, 26.8 mm for JJM5, 28 mm for 9023, and 27.7 mm for 6726. The general linear model that was run used a $\gamma$ distribution because of the positive skew in the data. The AICcmodavg package was used to compare the glm models and select the best fit model. This model included the individual parameter bacteria but eliminated the layer or interaction between bacteria/layer. Specific $p$-values can be seen in Table S3 for the glm output and Table S4 for the emmeans contrast results.

Results from the general linear model demonstrated that were significant differences in AgNP performance between 6726, PA01, and PA14. Pairwise comparisons were conducted using emmeans analysis to further explore whether significant differences resulted between each set of bacterial pairs, as shown in Table S5. Overall, there was no difference in AgNP performance between the *S. aureus* strains 6726 and 9023 and the *E. coli* strain MG1655. There were, however, significant differences between how AgNPs affected bacterial strains PA01 and PA14 when compared to the other three bacteria.

Overall, these data demonstrate similar NP performance in the *S. aureus* and *E. coli* strains (emmeans analysis, $p$-value > 0.05). Gram-negative strains PA01 and PA14 were more susceptible to AgNPs than their Gram-positive counterparts (emmeans analysis, $p$-values < 0.05) and an additional Gram-negative *E. coli* strain MG1655 ($p$-values < 0.05). A significant difference also existed between the effect of AgNPs on PA14 when compared to PA01 ($p$-value < 0.05). Finally, no significant difference was noted between *S. aureus* strains 9023 and 6726. Taken together, the comparative analysis suggests that AgNPs are more effective against both *Pseudomonas* strains than the other three bacterial strains in this study, with the greatest impact on *P. aeruginosa* strain PA14. More detailed information on the stats script used for the statistical analysis is given in Figure S18.

Explanations for the differences or lack thereof in coating performance against these microbial strains could be related to several variables. Characteristics of NPs including particle size, surface charge, concentration, diffusibility, and even the presence of oxidation can impact antimicrobial activity.[25,27,28] Mutations in porin proteins, competency of DNA repair mechanisms, microbial strain growth, and resistance profiles could also account for observed differences.[26] Differences notwithstanding, disk diffusion tests were done with colony-


https://doi.org/10.1021/acsami.2c01195
ACS Appl. Mater. Interfaces XXXX, XXX, XXX−XXX

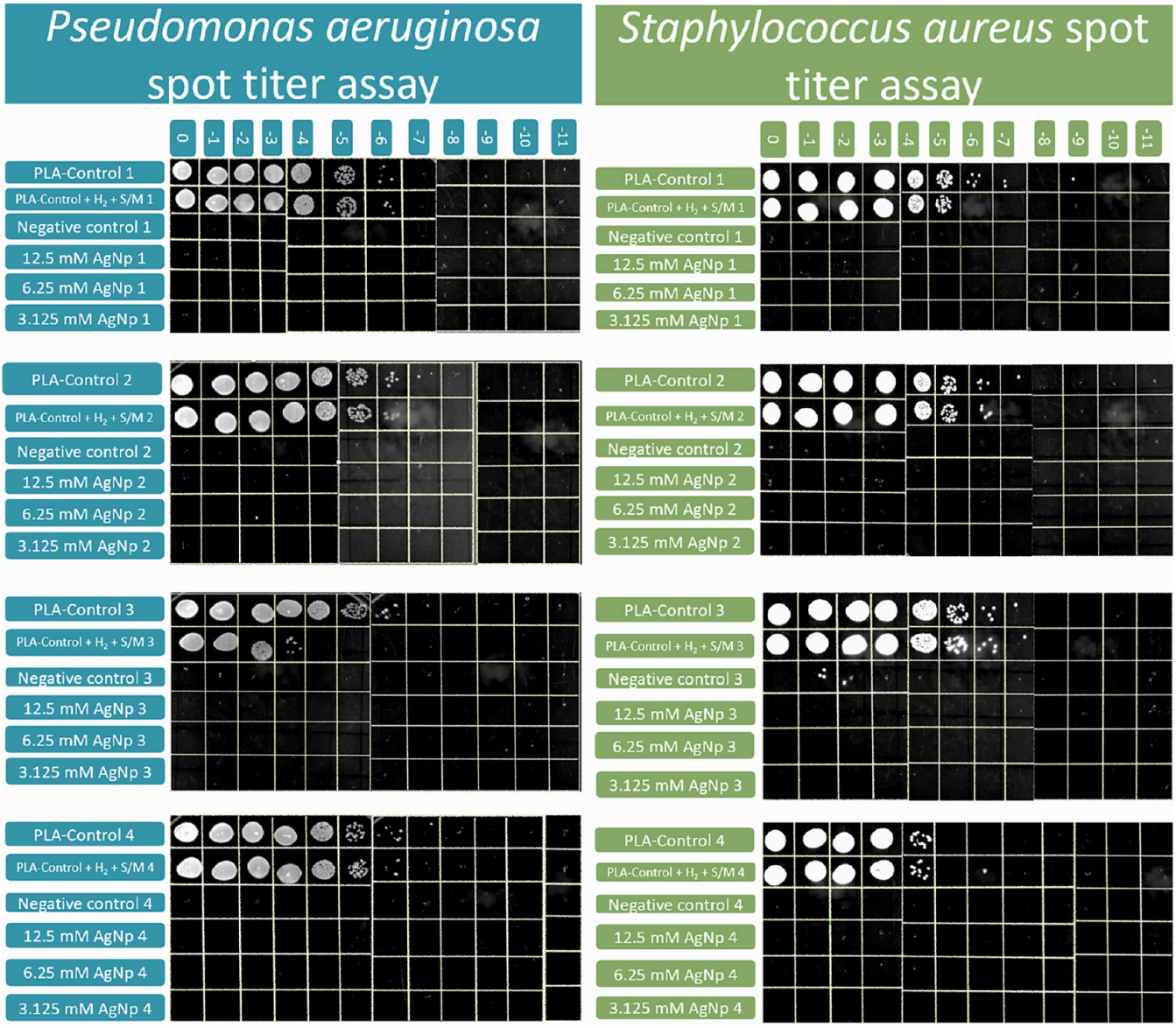


**Figure 10.** Spot titer assay showing dilution series for PA14 and 9023. Each image is a set of replicates. Labels along the side indicate the scaffold type (control or treatment), and the labels along the top indicate the dilution. The most remarkable item of note is the complete absence of bacterial growth for all the AgNP concentrations tested. The eight negative controls were negative for bacterial contamination as well.

forming unit (cfu) concentrations higher than would be found in natural systems (with the exception of established infection), implying that these coatings have the capability to be used across multiple industries as antimicrobials.

In addition to disk diffusion studies, we evaluated the antibacterial performance of 3D printed PLA scaffolds modified with AgNP coating using inhibitory concentration testing. Initially, we evaluated the efficacy of 250 mM AgNP-modified scaffolds (which were neither sonicated nor medium-soaked) using the spot titer assay (Figure S19). Raw cell density counts for both bacterial strains (*P. aeruginosa* strain PA14 and methicillin-resistant *S. aureus* strain 9023) can be seen in Tables S6 and S7 in the Supporting Information *P. aeruginosa* strain PA14 inactivation was demonstrated in wells with the 250 mM AgNP-treated scaffolds by the absence of growth for all titer dilutions. Conversely, control scaffolds had an average density of $1.5 \times 10^{10}$ cfu/mL, slightly higher than the positive control cell density at $1.2 \times 10^{9}$ cfu/mL. For methicillin-resistant *S. aureus* strain 9023, the mean cfu/mL for 250 mM AgNP-treated scaffolds was $7.3 \times 10^{5}$. Two of the three control scaffolds for 9023 were contaminated, so these were not considered. The single remaining control scaffold cell density was $1.6 \times 10^{10}$ cfu/mL, which was close to the positive control cell density of $1.4 \times 10^{10}$ cfu/mL.

Subsequently, we tested the antibacterial potential of three lower concentrations of AgNP-modified scaffolds (12.5, 6.25, and 3.12 mM) which were found to be the most cytocompatible as per our MTT assay. We also included additional PLA control scaffolds, which were modified with hydrogen plasma in this testing. The rationale for this was to assess any antibacterial capability attributable to the hydrogen plasma treatment itself. The results and the raw data from this testing can be seen in Figure 10 and Tables S8–S10. *P. aeruginosa* strain PA14 was completely inactivated by AgNP-treated scaffolds, demonstrated by the absence of growth for all titer dilutions. Both types of control scaffolds (pristine and


https://doi.org/10.1021/acsami.2c01195
ACS Appl. Mater. Interfaces XXXX, XXX, XXX−XXX

hydrogen plasma-modified PLA scaffolds) demonstrated robust bacterial growth. PLA control scaffolds had an average cell density of $1.3 \times 10^9$ cfu/mL. Hydrogen plasma-treated PLA controls had an average cell density of $9.3 \times 10^8$ cfu/mL. This clearly suggests that the pristine and hydrogen plasma-treated PLA scaffolds have no antibacterial activity.

Spot titer assay results obtained for *P. aeruginosa* strain PA14 were similar for all four AgNP (250, 12.5, 6.2, and 3.12 mM)-modified scaffolds. Interestingly, the same is not true for our *S. aureus* strain. For this strain, we observed total inactivation for the lowest concentrations of AgNPs (12.5, 6.2, and 3.12 mM), as opposed to a 5-fold decrease in the bacterial cell growth between the control and the treated scaffolds for the 250 mM concentration. Meanwhile, the PLA control and PLA hydrogen plasma-treated scaffolds had mean cell densities of $7.1 \times 10^8$ and $2 \times 10^9$ cfu/mL, respectively.

Given *P. aeruginosa* strain PA14 susceptibility in the mask testing, it comes as no surprise that it would be well inhibited by a AgNP-coated scaffold. The difference, however, in antibacterial performance in *S. aureus* is interesting. It is quite possible that the difference in inoculating cell densities allowed the lower AgNP concentrations to completely kill off bacteria before a stable culture could arise. Potential implications of this phenomenon are that utilizing AgNP coatings at the onset is more likely to prevent bacterial growth to cell densities that would subsequently cause infection.

Of course, the observed variability in AgNP performance against 9023 may also be attributed to differences in the stability and attachment of the AgNPs on the surface of the scaffold. It was already known that AgNPs are highly charged and tend to aggregate in solution.[29] Our 250 mM AgNP-modified scaffolds were unsonicated and unsoaked, resulting in abundant less stably attached NPs. These loosely attached NPs and unreacted silver salts bled into the surrounding environment, as evidenced by immediate turbidity of the solution when the scaffolds were placed in clear media (potentially causing aggregates to form). This turbidity upon contact was not observed with the sonicated soaked scaffolds. This clearly suggests that lower AgNP concentrations can be as, if not more, effective to combat bacterial infection. We assume that in the case of lower concentrations of the AgNP-modified scaffold, the antibacterial performance is accomplished via contact killing of the microbes by AgNPs.[30] Two final explanations are either a phenotypic shift or a genetic mutation which gave bacteria immunity to AgNPs. Higher concentrations of AgNPs create a highly selective environment which could give rise to resistant mutants very quickly. Alternatively, mutations commonly result from the bottleneck events, of which culture transfer is an example. The bacteria tested against the lower AgNP concentrations had been passaged three times, potentially causing decreased strain fitness in the NP-containing environment, leading to cell death. Additional experiments to explore these assumptions are a valuable and fascinating addition to our future work. Taken as a whole, however, these results tentatively establish AgNP coating efficacy in a planktonic system against Gram-negative bacteria. It is also evident that under certain conditions, the AgNPs can combat Gram-positives. There does appear to be greater AgNP inhibition of bacterial growth in solution than within a diffusional environment. This can be explained by considering that planktonic systems under agitation offer greater opportunity for *k* interactions between the solubilized NPs and bacterial cells. Differences in gene expression (planktonic vs biofilm) and the protection afforded within a biofilm can also account for the disparity between habitat-associated levels of growth inhibition.[28,31] These findings suggest that the AgNP coating could be applied to multiple surfaces to prevent bacterial colonization and infection. In summary, the antibacterial studies clearly support the strong antibacterial efficacy of silver nanostructures formed on the surface of both surgical mask layers and 3D printed polymeric scaffolds.

There are many different recent reports on the modification of 3D printed scaffolds with metallic NPs for antibacterial applications.[32−34] These methods require multiple steps and need different reagents to form/add metallic NP coatings on the surface of 3D scaffolds and therefore cannot be applied to all the different hydrophobic and hydrophilic 3D printed scaffolds. In comparison with all these recent approaches to nanostructure metallic NPs on 3D scaffolds, our PER process is a robust, safe, and scalable method which can be applied to modify the surface of any 3D printed scaffolds, regardless of any of its properties. More importantly, we were able to optimize this PER process to generate uniform metallic NP-modified scaffolds while simultaneously improving their cytocompatibility. This is very important for the clinical translation of nanostructured polymers for different biomedical applications.

## 4. CONCLUSIONS

In conclusion, we report an efficient, green PER method for generating metallic nanostructures on the surface of fibrous and 3D printed polymeric substrates. The reported method has the following advantages (i) eliminates toxic byproducts of the reduction process, (ii) is fast, economical, and easily scalable in industry settings, and (iii) is applicable for *in situ* surface modification of a breadth of hydrophilic and hydrophobic polymer surfaces. These metallic nanostructures, especially the AgNP coating on surgical mask layers and 3D printed polymer scaffolds have clear antibacterial competence against Gram-negative and Gram-positive bacteria responsible for causing infection. More importantly, we were able to optimize this PER process to generate uniform AgNP-modified scaffolds while simultaneously improving cytocompatibility. Considering the current pandemic and the possibility of future calamities, in conjunction with the rise in antibiotic resistance, there is a clear justification for developing novel approaches for biointerface surface modification. We hope that the proposed PER process will find wide utility to design metallic nanostructured interfaces for different biomedical applications such as SERS-based biosensing and bone tissue engineering. Our future studies aim to use this method toward the development of low-cost cellulose filter paper-based SERS biosensors and the development of metallic NP-modified 3D printed polymer scaffolds as bone−tissue interfacial scaffolds for osteomyelitis.

## ■ ASSOCIATED CONTENT

### Supporting Information

The Supporting Information is available free of charge at https://pubs.acs.org/doi/10.1021/acsami.2c01195.

Photographs of the AgNP- and AuNP-modified cellulose papers, XPS spectrum of the AgNP- and AuNP-modified cellulose papers, XPS spectrum of the AgNP-modified face mask, SEM and EDAX mapping of AgNP- and AuNP-modified 3D printed PLA scaffolds, ICP−MS analysis of the AgNP-modified 3D PLA scaffolds, raw



https://doi.org/10.1021/acsami.2c01195
ACS Appl. Mater. Interfaces XXXX, XXX, XXX−XXX

DOI measurements for different layers of the face mask M1 and M3, coefficient results from the general linear model, results from the emmeans analysis, contrast results from the pairwise emmeans analysis, detailed description of the R script used for the statistical analysis, pictures of the spot testing results for the 3D scaffold testing, calculations of the bacterial cell densities (cfu/mL) on 3D scaffolds, layout of the 3D scaffold incubation plate, and detailed protocol of inhibitory concentration testing on 3D printed scaffolds (PDF)

## AUTHOR INFORMATION


### Corresponding Author

**Vinoy Thomas** − *Department of Materials Science and Engineering, Laboratory for Polymers & Healthcare Materials/Devices, The University of Alabama at Birmingham (UAB), Birmingham, Alabama 35233, United States; Center for Nanoscale Materials and Bio-integration (CNMB), The University of Alabama at Birmingham (UAB), Birmingham, Alabama 35294, United States;* orcid.org/0000-0002-1191-3353; Email: vthomas@uab.edu

### Authors

**Vineeth M. Vijayan** − *Department of Materials Science and Engineering, Laboratory for Polymers & Healthcare Materials/Devices, The University of Alabama at Birmingham (UAB), Birmingham, Alabama 35233, United States; Center for Nanoscale Materials and Bio-integration (CNMB), The University of Alabama at Birmingham (UAB), Birmingham, Alabama 35294, United States;* orcid.org/0000-0003-4764-8085

**Melissa Walker** − *Department of Biology, The University of Alabama at Birmingham (UAB), Birmingham, Alabama 35233, United States*

**Renjith R. Pillai** − *Department of Materials Science and Engineering, Laboratory for Polymers & Healthcare Materials/Devices, The University of Alabama at Birmingham (UAB), Birmingham, Alabama 35233, United States*

**Gerardo Hernandez Moreno** − *Department of Materials Science and Engineering, Laboratory for Polymers & Healthcare Materials/Devices, The University of Alabama at Birmingham (UAB), Birmingham, Alabama 35233, United States*

**Yogesh K. Vohra** − *Center for Nanoscale Materials and Bio-integration (CNMB), The University of Alabama at Birmingham (UAB), Birmingham, Alabama 35294, United States*

**J. Jeffrey Morris** − *Department of Biology, The University of Alabama at Birmingham (UAB), Birmingham, Alabama 35233, United States*

Complete contact information is available at: https://pubs.acs.org/10.1021/acsami.2c01195


### Author Contributions

V.M.V. and M.W. contributed equally to this work. The manuscript was written through contributions of all authors. All authors have given approval to the final version of the manuscript.


### Funding

This work was supported by funding through NSF EPSCoR RII-Track-1 Cooperative agreement OIA-1655280. V.M.V. thanks for the seed research grant funding from the UAH/NSF CPU2AL program. V.T. and R.R.P. also acknowledge the financial support by P42-ES027723-01A1 from the NIEHS of the US National Institutes of Health (NIH) Superfund Research Program (SRP) grant. M.W. acknowledges the support of the National Science Foundation Graduate Research Fellowship program through grant DGE-1945997. Any statement, opinion, recommendation, or conclusions shared are those only of the authors and do not necessarily relay the official positions of the US National Science Foundation (NSF) or NIH.


### Notes

The authors declare no competing financial interest.


## ACKNOWLEDGMENTS

The authors thank Dr. Paul Baker, Director of Advanced Materials Characterization Core, UAB, for XPS and SEM imaging and Evan Eltinge, Keyence Corporation of America, for the 3D laser scanning confocal microscopy surface analysis. They also thank Prof. Suzanne Lapi and James Mokaya of the UAB Department of Radiology for their technical assistance in conducting analysis by ICP−MS.


## ABBREVIATIONS

PER, plasma electroless reduction
LTP, low-temperature plasma
AgNPs, silver nanoparticles
AuNPs, gold nanoparticles
PLA, polylactic acid
LTHPT, low-temperature hydrogen plasma treatment
LTAPT, low-temperature air plasma treatment
XPS, X-ray photoelectron spectroscopy
SEM, scanning electron microscopy
EDAX, energy-dispersive X-ray spectroscopy
TEM, transmission electron microscopy
SERS, surface-enhanced Raman spectroscopy
*E. coli*, *Escherichia coli*
CFU, colony-forming unit

## REFERENCES


(1) Yaqoob, S. B.; Adnan, R.; Rameez Khan, R. M.; Rashid, M. Gold, Silver, and Palladium Nanoparticles: A Chemical Tool for Biomedical Applications. *Front. Chem.* **2020**, *8*, 376.

(2) Sánchez-López, E.; Gomes, D.; Esteruelas, G.; Bonilla, L.; Lopez-Machado, A. L.; Galindo, R.; Cano, A.; Espina, M.; Ettcheto, M.; Camins, A.; Silva, A. M.; Durazzo, A.; Santini, A.; Garcia, M. L.; Souto, E. B. Metal-Based Nanoparticles as Antimicrobial Agents: An Overview. *Nanomaterials* **2020**, *10*, 292.

(3) Eivazzadeh-Keihan, R.; Bahojb Noruzi, E.; Khanmohammadi Chenab, K.; Jafari, A.; Radinekiyan, F.; Hashemi, S. M.; Ahmadpour, F.; Behboudi, A.; Mosafer, J.; Mokhtarzadeh, A.; Maleki, A.; Hamblin, M. R. Metal-based nanoparticles for bone tissue engineering. *J. Regen. Med. Tissue Eng.* **2020**, *14*, 1687−1714.

(4) Joseph, M. M.; Narayanan, N.; Nair, J. B.; Karunakaran, V.; Ramya, A. N.; Sujai, P. T.; Saranya, G.; Arya, J. S.; Vijayan, V. M.; Maiti, K. K. Exploring the Margins of SERS in Practical Domain: An Emerging Diagnostic Modality for Modern Biomedical Applications. *Biomaterials* **2018**, *181*, 140−181.

(5) Palza, H. Antimicrobial Polymers with Metal Nanoparticles. *Int. J. Mol. Sci.* **2015**, *16*, 2099−2116.

(6) Thomas, V.; Yallapu, M. M.; Sreedhar, B.; Bajpai, S. K. A Versatile Strategy to Fabricate Hydrogel−Silver Nanocomposites and Investigation of Their Antimicrobial Activity. *J. Colloid Interface Sci.* **2007**, *315*, 389−395.
(7) Triebel, C.; Vasylyev, S.; Damm, C.; Stara, H.; Özpınar, C.; Hausmann, S.; Peukert, W.; Münstedt, H. Polyurethane/Silver-Nanocomposites with Enhanced Silver Ion Release Using Multifunctional Invertible Polyesters. *J. Mater. Chem.* **2011**, *21*, 4377.
(8) Pereira, S.; Barros-Timmons, A.; Trindade, T. Polymer@gold Nanoparticles Prepared via RAFT Polymerization for Opto-Biodetection. *Polymers* **2018**, *10*, 189.
(9) Pishbin, F.; Mouriño, V.; Gilchrist, J. B.; McComb, D. W.; Kreppel, S.; Salih, V.; Ryan, M. P.; Boccaccini, A. R. Single-Step Electrochemical Deposition of Antimicrobial Orthopaedic Coatings Based on a Bioactive Glass/Chitosan/Nano-Silver Composite System. *Acta Biomater.* **2013**, *9*, 7469−7479.
(10) Mazloomi-Rezvani, M.; Salami-Kalajahi, M.; Roghani-Mamaqani, H. Grafting to" Approach for Surface Modification of AuNPs with RAFT-Mediated Synthesized Smart Polymers: Stimuli-Responsive Behaviors of Hybrid Nanoparticles. *J. Phys. Chem. Solids* **2018**, *123*, 183−190.
(11) Huang, X.; Hu, J.; Li, Y.; Xin, F.; Qiao, R.; Davis, T. P. Engineering Organic/Inorganic Nanohybrids through RAFT Polymerization for Biomedical Applications. *Biomacromolecules* **2019**, *20*, 4243−4257.
(12) Richmonds, C.; Sankaran, R. M. Plasma-Liquid Electrochemistry: Rapid Synthesis of Colloidal Metal Nanoparticles by Microplasma Reduction of Aqueous Cations. *Appl. Phys. Lett.* **2008**, *93*, 131501.
(13) Tasche, D.; Weber, M.; Mrotzek, J.; Gerhard, C.; Wieneke, S.; Möbius, W.; Höfft, O.; Viöl, W. In Situ Investigation of the Formation Kinematics of Plasma-Generated Silver Nanoparticles. *Nanomaterials* **2020**, *10*, 555.
(14) Sun, D.; McLaughlan, J.; Zhang, L.; Falzon, B. G.; Mariotti, D.; Maguire, P.; Sun, D. Atmospheric Pressure Plasma-Synthesized Gold Nanoparticle/Carbon Nanotube Hybrids for Photothermal Conversion. *Langmuir* **2019**, *35*, 4577−4588.
(15) Kumari, S.; Chatterjee, K. Biomaterials-Based Formulations and Surfaces to Combat Viral Infectious Diseases. *APL Bioeng.* **2021**, *5*, 011503.
(16) Pemmada, R.; Zhu, X.; Dash, M.; Zhou, Y.; Ramakrishna, S.; Peng, X.; Thomas, V.; Jain, S.; Nanda, H. S. Science-Based Strategies of Antiviral Coatings with Viricidal Properties for the COVID-19 Like Pandemics. *Materials* **2020**, *13*, 4041.
(17) Mohiti-Asli, M.; Molina, C.; Diteepeng, T.; Pourdeyhimi, B.; Loboa, E. G. Evaluation of Silver Ion-Releasing Scaffolds in a 3D Coculture System of MRSA and Human Adipose-Derived Stem Cells for Their Potential Use in Treatment or Prevention of Osteomyelitis. *Tissue Eng., Part A* **2016**, *22*, 1258−1263.
(18) Sharma, R.; Dhillon, A.; Kumar, D. Mentha-Stabilized Silver Nanoparticles for High-Performance Colorimetric Detection of Al(III) in Aqueous Systems. *Sci. Rep.* **2018**, *8*, 5189.
(19) Sylvestre, J.-P.; Kabashin, A. V.; Sacher, E.; Meunier, M.; Luong, J. H. T. In *Nanoparticle Size Reduction during Laser Ablation in Aqueous Solutions of Cyclodextrins*; Herman, P. R., Fieret, J., Pique, A., Okada, T., Bachmann, F. G., Hoving, W., Washio, K., Xu, X., Dubowski, J. J., Geohegan, D. B., Traeger, F., Eds.; San Jose: Ca, 2004; p 84.
(20) Yang, J.; Zeng, Z.; Kang, J.; Betzler, S.; Czarnik, C.; Zhang, X.; Ophus, C.; Yu, C.; Bustillo, K.; Pan, M.; Qiu, J.; Wang, L. W.; Zheng, H. Formation of Two-Dimensional Transition Metal Oxide Nanosheets with Nanoparticles as Intermediates. *Nat. Mater.* **2019**, *18*, 970−976.
(21) Chen, Y.; Fan, Z.; Zhang, Z.; Niu, W.; Li, C.; Yang, N.; Chen, B.; Zhang, H. Two-Dimensional Metal Nanomaterials: Synthesis, Properties, and Applications. *Chem. Rev.* **2018**, *118*, 6409−6455.
(22) Krásný, I.; Kupská, I.; Lapčík, L. Effect of Glow-Discharge Air Plasma Treatment on Wettability of Synthetic Polymers. *J. Surf. Eng. Mater. Adv. Technol.* **2012**, *02*, 142−148.
(23) Vijayan, V. M.; Tucker, B. S.; Dimble, P. S.; Vohra, Y. K.; Thomas, V. Dusty-Plasma-Assisted Synthesis of Silica Nanoparticles for in Situ Surface Modification of 3D-Printed Polymer Scaffolds. *ACS Appl. Nano Mater.* **2020**, *3*, 7392−7396.
(24) Cámara-Torres, M.; Sinha, R.; Scopece, P.; Neubert, T.; Lachmann, K.; Patelli, A.; Mota, C.; Moroni, L. Tuning Cell Behavior on 3D Scaffolds Fabricated by Atmospheric Plasma-Assisted Additive Manufacturing. *ACS Appl. Mater. Interfaces* **2021**, *13*, 3631−3644.
(25) Ruparelia, J. P.; Chatterjee, A. K.; Duttagupta, S. P.; Mukherji, S. Strain Specificity in Antimicrobial Activity of Silver and Copper Nanoparticles. *Acta Biomater.* **2008**, *4*, 707−716.
(26) Arciola, C. R.; Campoccia, D.; Montanaro, L. Implant Infections: Adhesion, Biofilm Formation and Immune Evasion. *Nat. Rev. Microbiol.* **2018**, *16*, 397−409.
(27) Joo, S. H.; Aggarwal, S. Factors Impacting the Interactions of Engineered Nanoparticles with Bacterial Cells and Biofilms: Mechanistic Insights and State of Knowledge. *J. Environ. Manage.* **2018**, *225*, 62−74.
(28) Sondi, I.; Salopek-Sondi, B. Silver Nanoparticles as Antimicrobial Agent: A Case Study on E. Coli as a Model for Gram-Negative Bacteria. *J. Colloid Interface Sci.* **2004**, *275*, 177−182.
(29) Kędziora, A.; Speruda, M.; Krzyżewska, E.; Rybka, J.; Łukowiak, A.; Bugla-Płoskońska, G. Similarities and Differences between Silver Ions and Silver in Nanoforms as Antibacterial Agents. *Int. J. Mol. Sci.* **2018**, *19*, 444.
(30) Agnihotri, S.; Mukherji, S.; Mukherji, S. Immobilized silver nanoparticles enhance contact killing and show highest efficacy: elucidation of the mechanism of bactericidal action of silver. *Nanoscale* **2013**, *5*, 7328−7340.
(31) Gherasim, O.; Puiu, R. A.; Bîrcă, A. C.; Burduşel, A.-C.; Grumezescu, A. M. An Updated Review on Silver Nanoparticles in Biomedicine. *Nanomaterials* **2020**, *10*, 2318.
(32) Li, J.; Li, L.; Zhou, J.; Zhou, Z.; Wu, X.-l.; Wang, L.; Yao, Q. 3D printed dual-functional biomaterial with self-assembly micro-nano surface and enriched nano argentum for antibacterial and bone regeneration. *Appl. Mater. Today* **2019**, *17*, 206−215.
(33) Radhakrishnan, S.; Nagarajan, S.; Belaid, H.; Farha, C.; Iatsunskyi, I.; Coy, E.; Soussan, L.; Huon, V.; Bares, J.; Belkacemi, K.; Teyssier, C.; Balme, S.; Miele, P.; Cornu, D.; Kalkura, N.; Cavaillès, V.; Bechelany, M. Fabrication of 3D printed antimicrobial polycaprolactone scaffolds for tissue engineering applications. *Mater. Sci. Eng., C* **2021**, *118*, 111525.
(34) Rodríguez-Contreras, A.; Torres, D.; Rafik, B.; Ortiz-Hernandez, M.; Ginebra, M. P.; Calero, J. A.; Manero, J. M.; Ruperez, E. Bioactivity and antibacterial properties of calcium- and silver-doped coatings on 3D printed titanium scaffolds. *Surf. Coat. Technol.* **2021**, *421*, 127476.


https://doi.org/10.1021/acsami.2c01195
ACS Appl. Mater. Interfaces XXXX, XXX, XXX−XXX